PAPER

Check for updates

Mo(VI) complexes of amide–imine conjugates for tuning the selectivity of fluorescence recognition of Y(III) *vs.* Pb(II)†

Sudeshna Chatterjee, Sabyasachi Ta, (ID) Somnath Khanra and Debasis Das (ID) *

Two amide–imine conjugates, *viz.* 3-methyl-benzoic acid (4-diethylamino-2-hydroxy-benzylidene)-hydrazide (**L1**) and 3-methyl-benzoic acid (2-hydroxy-naphthalen-1-ylmethylene)-hydrazide (**L2**), have been prepared and used for a further synthesis of Mo(VI) complexes (**M1** and **M2**, respectively). Single crystal X-ray diffraction analysis confirmed their structures. Interestingly, **M1** selectively recognizes Y^{3+} and Pb^{2+} at two different wavelengths, whereas **M2** selectively interacts with Y^{3+} with a significantly high binding constant, 1.3×10^5 M^{-1}. The proposed sensing mechanism involves the displacement of Mo(VI) by Y^{3+}/Pb^{2+} from respective Mo(VI) complexes. The TCSPC experiment also substantiates the "turn-on" fluorescence process. A logic gate has been constructed utilizing the fluorescence recognition of cations by **M1**. DFT studies corroborated the cation–probe interactions and allowed exploring the orbital energy parameters.

Introduction

Yttrium, a mushy, luminous, and crystalline group III transition metal having similarities with lanthanides, has historically been grouped as a rare-earth metal[1] and has always been found in nature along with rare-earth minerals.[2] Chemically, yttrium favours lanthanides more intimately than neighbouring scandium.[3,4] Yttrium isotopes are the most common products in nuclear fission. Though yttrium is found in several uranium ores, it is rarely found in a free state.[5] Yttrium plays an important role in the replacement of thorium and as a catalyst for ethylene polymerization.[6,7] Water-soluble yttrium compounds are toxic that affect the lungs, kidney, spleen, and liver.[8] Radio-yttrium (yttrium-90, β-emitter) is used for the treatment of various cancers.[9] Thus, trace-level detection and determination of yttrium are highly demanding.

On the other hand, lead, the most noxious among heavy metals,[10–14] causes serious health issues through contaminated food, water, and air.[15,16] It affects the mucous tissues, intestines, bones, central nervous system, liver, kidney, and reproductive system. Even at very low concentrations, it disrupts the biosynthesis of haemoglobin to cause anemia.[17–19] World Health Organization (WHO) has listed Pb(II) among ten elements as

crucial to public health anxiety.[20] Thus, precise quantification of trace level Pb(II) is also a priority. Hence, we have explored a facile, rapid, inexpensive, non-invasive method such as fluorescence for the selective detection and quantification of Y(III) and Pb(II).

Metal displacement reactions are primarily employed in organometallic synthesis and catalytic cross-coupling reactions such as Suzuki, Stille, Negishi, and Sonogashira reactions.[21–35] Recently, we have employed the "metal displacement approach"[36–39] for easy optical recognition of cations.

For this purpose, the design of the probe is very crucial. Recently, we have focussed on the development of Mo(VI) complexes of amide–imine conjugates. The amide functionality has received notable attention in pharmaceutical formulations for its stability, conformational diversity, and high polarity.[40,41] Almost one-fourth of drug molecules and proteins contain amide as an active functional group.[42]

On the other hand, molybdenum is a cofactor of several enzymes, *viz.* nitrogenase, aldehyde oxidase, xanthine oxidase, sulphite oxidase, nitrate reductase, and xanthine dehydrogenase.[43] *Oxo*-molybdenum(VI) complexes have interesting stereochemical and microelectronic properties[44] having therapeutic and catalytic applications, possibly due to their switching ability amongst various oxidation states.[45]

As far as the literature is concerned, reports on simultaneous, selective optical recognition of Y^{3+} and Pb^{2+} are unavailable. Only a very few reports on Y^{3+} coordination chemistry/extraction are available.[46–50] A zinc porphyrin–CONH–quinone dyad (ZnP–CONH–Q) has been reported by Fukuzumi *et al.* for the detection of Y^{3+} in toxic benzonitrile medium, having a very low association constant.[51] On the other hand,

Department of Chemistry, The University of Burdwan, Burdwan, 713104, W.B., India. E-mail: ddas100in@yahoo.com; Fax: +91-342-2530452; Tel: +91-342-2533913, ext. 424

optical probes for selective detection of Pb^{2+} are few and involve either metal–organic frameworks/rhodamine derivatives.[52–55]

From a practical point of view, a single sensor that shows differential response towards multiple ions is more desirable over one-to-one sensors. These facts stimulated us to search for a single probe that can selectively detect both Y^{3+} and Pb^{2+}.

To address the lacunas and overcome the limitations, herein, we present two molecular probes, **M1**, capable of dual sensing Y^{3+} and Pb^{2+}, whereas **M2** recognizes only Y^{3+} in aqueous ethanol medium with improved binding constant and detection limit. Selectivity is achieved by tuning the probe backbone from substituted aniline to naphthalene (electronic control). **M1** and **M2** are two different molybdenum(VI) complexes of two amide–imine conjugates (**L1** and **L2**) synthesized by condensing *meta*-toluic acid hydrazide (**MTA**) with 4-(*N,N′*-diethylamino)salicylaldehyde and 2-hydroxy-1-naphthaldehyde, respectively. **MTA** is prepared from *m*-toluic acid *via* acid chloride and subsequently reacting with hydrazine.

The turn on fluorescence has been achieved *via* the *trans*-metalation/metal displacement approach, leading to **P1** and **Y2**, respectively. Kinetic studies unfold the molecular-level interaction and associated spectroscopic properties. The density functional theoretical (DFT) studies have substantiated the displacement mechanism. Emission wavelength based discrimination of Y^{3+} and Pb^{2+} using **M1** allowed the development of a binary logic gate that functions as a molecular switch.

Experimental

Methods and materials

Commercial reagents like HEPES buffer, 4-*N,N′*-diethylamino-salicylaldehyde, 2-hydroxy-naphthaldehyde, hydrazine hydrate, and metal salts have been purchased from Sigma-Aldrich and Merck. Spectroscopic grade solvents have been used. Shimadzu FTIR (model IR Prestige 21 CE) spectrometer is used to record FTIR spectra. PerkinElmer 2400 series II CHN analyzer was used for elemental analysis. Shimadzu UV-2450 spectrophotometer with a 1 cm path length quartz cell is used to record absorption spectra. A QTOF 60 Micro YA 263 mass spectrometer is employed to measure the mass spectra in the ES positive mode. Fluorescence spectra are recorded on a Hitachi F-7000 spec-trofluorimeter. A systronics digital pH meter (model 335) is used to measure the pH of the solution. A Bruker ADVANCE III HD (400 MHz) spectrometer is employed to record ^1H NMR spectra in DMSO-d_6 solvent. The chemical shift value (ppm) with residual solvent peak is used as an internal reference. Multiplicity is indicated as follows: s (singlet), d (doublet), t (triplet), q (quartet), and m (multiplet). Coupling constants (J, s) have been reported in Hertz (Hz). Fluorescence lifetime data have been collected by time correlated single photon counting (TCSPC) technique using FluoroCube-01-NL spectrometer using a Laser-diode (model: DD-450L-8666, typical FWHM ~170 ps). Kinetic measurements have been carried out with an Applied Photo physics SX 17MV stopped-flow spectrophotometer (model OPT-622) in the symmetric mixing mode at 25 °C and ambient pressure.

X-ray data are collected on a Bruker X8 APEX-II CCD diffractometer at 100(2) K using graphite-monochromated Mo K_α radiation (0.71073 Å) at 150 K. Data are processed and corrected for Lorentz and polarization absorption effects. Crystal structures were solved by standard direct methods using the SHELXS[56] and refined by full-matrix least-squares with SHELXL[57] and OLEX2,[58] software. Significant crystal parameters and refinement data are presented in Table S1 (ESI).† All non-hydrogen atoms are refined with anisotropic thermal displacements. Hydrogen atoms are not included in the structure factor calculation in geometrically idealized positions, with thermal parameters depending on the parent atom, using a riding model. Images are generated by Mercury software.[59]

Synthesis

3-Methyl-benzoic acid hydrazide (MTA). A few drops of $SOCl_2$ were added to the ethanol solution of *m*-toluic acid (1 g, 7.34 mmol) under stirring conditions at room temperature (Scheme 1). The resulting mixture was reacted with hydrazine hydrate to get the target hydrazide, MTA, with a 65% yield. Its molecular formula is $C_8H_{10}N_2O$ (MW = 150.18). Anal. found, C, 63.78; H, 6.61 and N, 18.83; calcd, C, 63.98; H, 6.71 and N, 18.65. ESI-MS(+) m/z [M + Na]$^+$, 172.82 (Fig. S1a, ESI†). ^1H NMR (Fig. S1b, ESI†), 400 MHz, DMSO-d_6, TMS, J (Hz), δ (ppm): 9.713 (1H, s), 7.636–7.589 (2H, m), 7.320–7.306 (2H, q), 4.470 (2H, s), 3.406 (3H, s). ^{13}CNMR (Fig. S1c, ESI†): 166.62, 138.13, 133.82, 132.21, 128.76–128.15, 124.57 and 21.82. FTIR (KBr, cm^{-1}): 3416, ν(N–
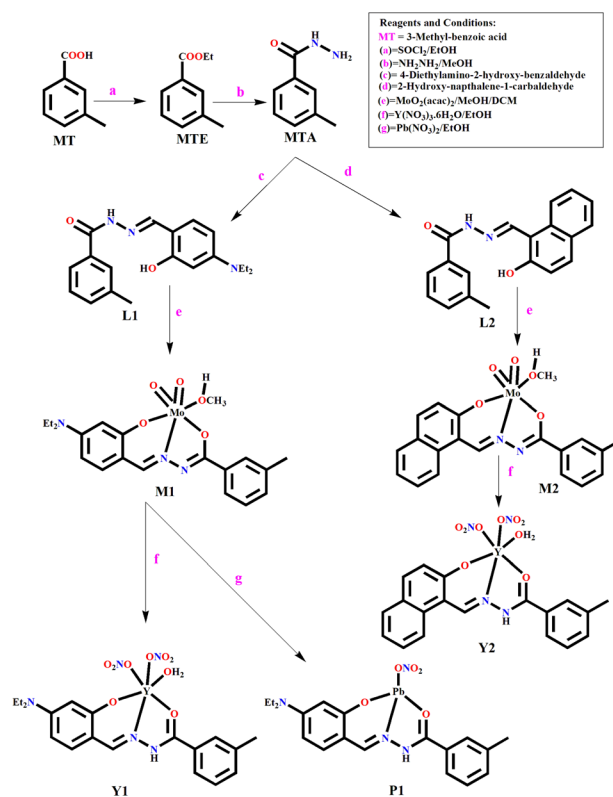
Scheme 1 Synthetic protocol of **MTA**, **M1**, **M2**, **Y1**, **P1**, and **Y2**.

H); 2908, ν(C–H, aromatic); 1675, ν(C=O); 1585, ν(C–H, aliphatic); 1189, ν(N–N) (Fig. S1d, ESI).†

3-Methyl-benzoic acid (4-diethylamino-2-hydroxy-benzylidene)-hydrazide (L1). A mixture of MTA (150 mg, 1.0 mmol) and 4-N,N'-diethylamino-salicylaldehyde (193 mg, 1.0 mmol) was refluxed in methanol for 6 h. Finally, the solution was kept for slow evaporation while the yellow compound, **L1** was collected with 81% yield after a few days (Scheme 1). Its molecular formula is $C_{19}H_{23}N_3O_2$ (MW = 325.40). Anal. found, C, 69.36; H, 7.70 and N, 12.06; calcd, C, 70.13; H, 7.12 and N, 12.91. ESI-MS (m/z): $[M + H]^+$, 326.48, $[M + Na]^+$, 348.49 (Fig. S2a, ESI†). ^1H NMR (DMSO-d_6, 400 MHz, J Hz, δ ppm):11.697 (1H, s), 11.405 (1H, s), 8.347 (1H, s), 7.653–7.619 (2H, t, J = 6.8 Hz), 7.348–7.334 (2H, d, J = 5.6 Hz), 7.130–7.109 (1H, d, J = 8.4 Hz), 6.217–6.195 (1H, t, J = 4.4 Hz), 6.058 (1H, s), 3.414 (3H, s), 3.301 (4H, s), 1.107–1.023 (7H, m) (Fig. S2b, ESI†). FTIR (KBr, cm^{-1}): 3237, ν(O–H); 2975, ν(C–H, aromatic); 1638, ν(C=O); 1526, ν(C=N); 1130, ν(N–N) (Fig. S2c, ESI†).

3-Methyl-benzoic acid-(2-hydroxy-naphthalen-1-ylmethylene)-hydrazide (L2). Methanol solution of MTA (150 mg, 1.0 mmol) and 2-hydroxy-1-naphthaldehyde (172 mg, 1.0 mmol) was refluxed for 2 h, and the resulting brown solution was kept for slow evaporation, while brown **L2** was collected at 76% yield after few days (Scheme 1). Its molecular formula is $C_{19}H_{16}N_2O_2$ (MW = 304.34). Anal. found, C, 74.20; H, 5.02 and N, 9.11; calcd, C, 74.98; H, 5.30 and N, 9.20. ESI-MS (m/z): $[M + H]^+$, 305.39; $[M + Na]^+$, 327.39 (Fig. S3a, ESI†). ^1H NMR (DMSO-d_6, 400 MHz, J Hz, δ ppm) 12.773 (1H, s), 12.115 (1H, s), 9.431 (1H, s), 8.174–8.152 (1H, d, J = 8.8 Hz), 7.894–7.838 (2H, m), 7.742–7.708 (2H, m), 7.580–7.542 (1H, m), 7.433–7.341 (3H, m), 7.195–7.172 (1H, d, J = 9.2 Hz), 3.301–3.235 (7H, t, J = 13.6 Hz) (Fig. S3b, ESI†). FTIR (KBr, cm^{-1}): 3192, ν(O–H); 3027, ν(C–H, aromatic); 1623, ν(C=O); 1570, ν(C=N); 1182, ν(N–N) (Fig. S3c, ESI†).

M1 and M2. Solutions of $MoO_2(acac)_2$ (1 g, 3.04 mmol, MeOH, 5 mL) were added separately to each of **L1** (0.5 g, 1.53 mmol, 10 mL) and **L2** (0.5 g, 1.64 mmol, 10 mL) in MeOH/DCM under stirring conditions for 2 h (Scheme 1). Slow evaporation of solvent yielded brown crystals of **M1** and **M2**, respectively.

M1: (yield, 68%), molecular formula is $C_{20}H_{25}MoN_3O_5$ (MW = 483.38). Anal. found, C, 49.21; H, 4.95 and N, 8.76; calcd, C, 49.70; H, 5.21 and N, 8.69. ESI-MS (m/z): $[M + H]^+$, 486.64 (Fig. S4a, ESI†). FTIR (KBr, cm^{-1}): 2923, ν(C–H, aromatic); 1646, ν(C=O); 1481, ν(C=N); 1078, ν(N–N) (Fig. S4b, ESI†). The structure of **M1** was confirmed by SC-XRD analysis.

M2: (yield, 62%), molecular formula is $C_{20}H_{18}MoN_2O_5$ (MW = 462.31). Anal. found, C, 51.11; H, 3.25 and N, 6.39; calcd, C, 51.96; H, 3.92 and N, 6.06. ESI-MS (m/z): $[M + 2H_2O + H]^+$, 500.96 (Fig. S5a, ESI†). FTIR (KBr, cm^{-1}): 3005, ν(C–H, aromatic); 1660, ν(C=O); 1563, ν(C=N); 1175, ν(N–N) (Fig. S5b, ESI†). The structure of **M2** was confirmed by SC-XRD analysis.

Y1 (M1-Y adduct), Y2 (M2-Y adduct) and P1 (M1-Pb adduct). In separate magnetically stirred methanol solutions of **M1** and **M2**, methanol solutions of Y(NO$_3$)$_3$·6H$_2$O were added drop-wise for 5 min. In another set, a methanol solution of Pb(NO$_3$)$_2$ was added to the solution of **M1** in methanol under stirring

conditions. The mixtures were kept for slow evaporation to yield **Y1, Y2,** and **P1,** respectively.

Y1: the yield was 52%, molecular formula is $C_{19}H_{24}N_5O_9Y$ (MW = 555.33). Anal. found, C, 42.09; H, 4.32 and N, 12.04; calcd, C, 41.09; H, 4.36 and N, 12.61. ESI-MS (m/z): $[M + H_2O]^+$, 573.0059 (Fig. S6a, ESI†) FTIR (KBr, cm^{-1}): 3349, ν(N–H); 3154, ν(C–H, aromatic); 1646, ν(C=O); 1476, ν(C=N) (Fig. S6b, ESI†).

Y2: the yield was 64%, molecular formula is $C_{19}H_{17}N_4O_9Y$ (MW = 534.27). Anal. found, C, 42.88; H, 3.41 and N, 10.94; calcd, C, 42.71; H, 3.21 and N, 10.49. ESI-MS (m/z): $[M + 2H_2O]^+$, 569.3079 (Fig. S7a, ESI†). FTIR (KBr, cm^{-1}): 3491, ν(N–H); 3162, ν(C–H, aromatic); 1623, ν(C=O); 1407, ν(C=N) (Fig. S7b, ESI†).

P1: the yield was 70%, molecular formula is $C_{19}H_{22}N_4O_5Pb$ (MW = 593.60). Anal. found, C, 38.46; H, 3.60 and N, 9.56; calcd, C, 38.44; H, 3.74 and N, 9.44. ESI-MS (m/z): $[M + H]^+$, 595.1094 (Fig. S8a, ESI†). FTIR (KBr, cm^{-1}): 3573, ν(N–H); 2766, ν(C–H, aromatic); 1630, ν(C=O); 1384, ν(C=N). (Fig. S8b, ESI†).

Results and discussion

X-ray diffraction analysis

The molecular structures of **M1** and **M2** were confirmed by single crystal X-ray diffraction analysis. Details of crystallographic refinement parameters are provided in Table S1 (ESI).† Selected bond lengths and angles are presented in Tables S2a and b (ESI),† respectively. Both the complexes, **M1** (CCDC 1941205) and **M2** (CCDC 1919499), show distorted octahedral geometry having identical molecular structures (Fig. 1).

In **M1**, bond lengths, O1–C1 (1.29(3) Å) and O2–C11 (1.34(3) Å) for phenol C–O bond and amide C–O bond are close, indicating the C–O single bond character. Thus, the C=O bond of amide in amide–imine conjugate has a single bond character after complexation with Mo(vi). A similar observation was made for the complex **M2** where O2–C11 (1.342(2) Å) for phenol C–O bond and O1–C1 (1.310(2) Å) for amide C–O bond were close enough. The C=N bond character is reflected from the bond length N1–C1 (1.28(3) Å) and N2–C9 (1.34(3) Å) in **M1** whereas bond lengths N1–C1 (1.311(2) Å) and N2–C9 (1.294(2) Å) indicate the double bond character of CH=N in **M2**.

Two *oxo* groups maintained a *cis*-geometry, with Mo=O double character in **M1**, Mo–O4 (1.69(2) Å) and Mo–O5 (1.727(16) Å) and **M2**, Mo–O3 (1.7046(15) Å) and Mo–O4 (1.6945(15) Å). Bond lengths Mo–O1 (2.012(13) Å) and Mo–O2 (1.925(15) Å) in **M1** and Mo–O1 (2.0093(14) Å) and Mo–O2 (1.9286(14) Å) in **M2** indicated Mo–O single bond character.

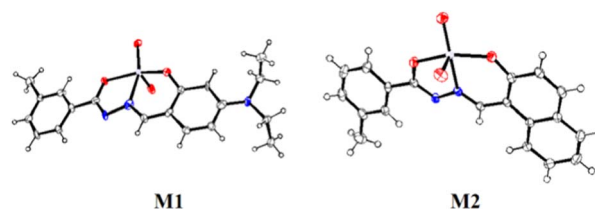Both the complexes adopted six co-ordination including methanol as coordinating solvent. Bond angles, O2–Mo–O1

Fig. 1 ORTEP view of **M1** and **M2** (50% ellipsoid probability).

(149.8(6)°), O4–Mo–O3 (170.3(8)°) and O5–Mo–N2 (158.2(9)°) in **M1** and O2–Mo–O1 (149.77(6)°), O5–Mo–O4 (171.28(6)°) and N2–Mo–O3 (155.41(7)°) in **M2** reveal distorted octahedral geometries.

Spectroscopic studies

Spectroscopic recognition of Y^{3+} and Pb^{2+} along with spectroscopic properties of **M1** and **M2** have been thoroughly investigated.

The ethanol solution of **L1** absorbs at 372 nm, assigned as n–π* electronic transition. Upon addition of Mo(VI) to **L1**, the absorbance increases significantly with a minor blue shift to 363 nm. This intensified optical density (OD) value is due to metal bound intra-ligand charge transfer (CT) process.

Upon the addition of Y^{3+}, the absorbance of **M1** at 363 nm in EtOH/H$_2$O (4/1, v/v) decreases significantly with the appearance of a new peak at 413 nm through an isosbestic point at 374 nm (Fig. 2a). This is due to the formation of the [**L1**-Y^{3+}] adduct *via* the metal displacement process that consequently affects the intra-ligand charge transfer process.

Similarly, upon the addition of Pb^{2+} to **M1**, the absorbance at 363 nm decreases with the appearance of a new peak at 426 nm with an isosbestic point at 396 nm (Fig. 2b).

On the other hand, the ethanol solution of **L2** absorbs at 320 nm and 360 nm, assigned to π–π* and n–π* transitions, respectively, which are intensified and shifted to 311 nm and 440 nm, respectively, upon the addition of Mo(VI), attributed to metal bound intra-ligand charge transfer (ILCT) process,
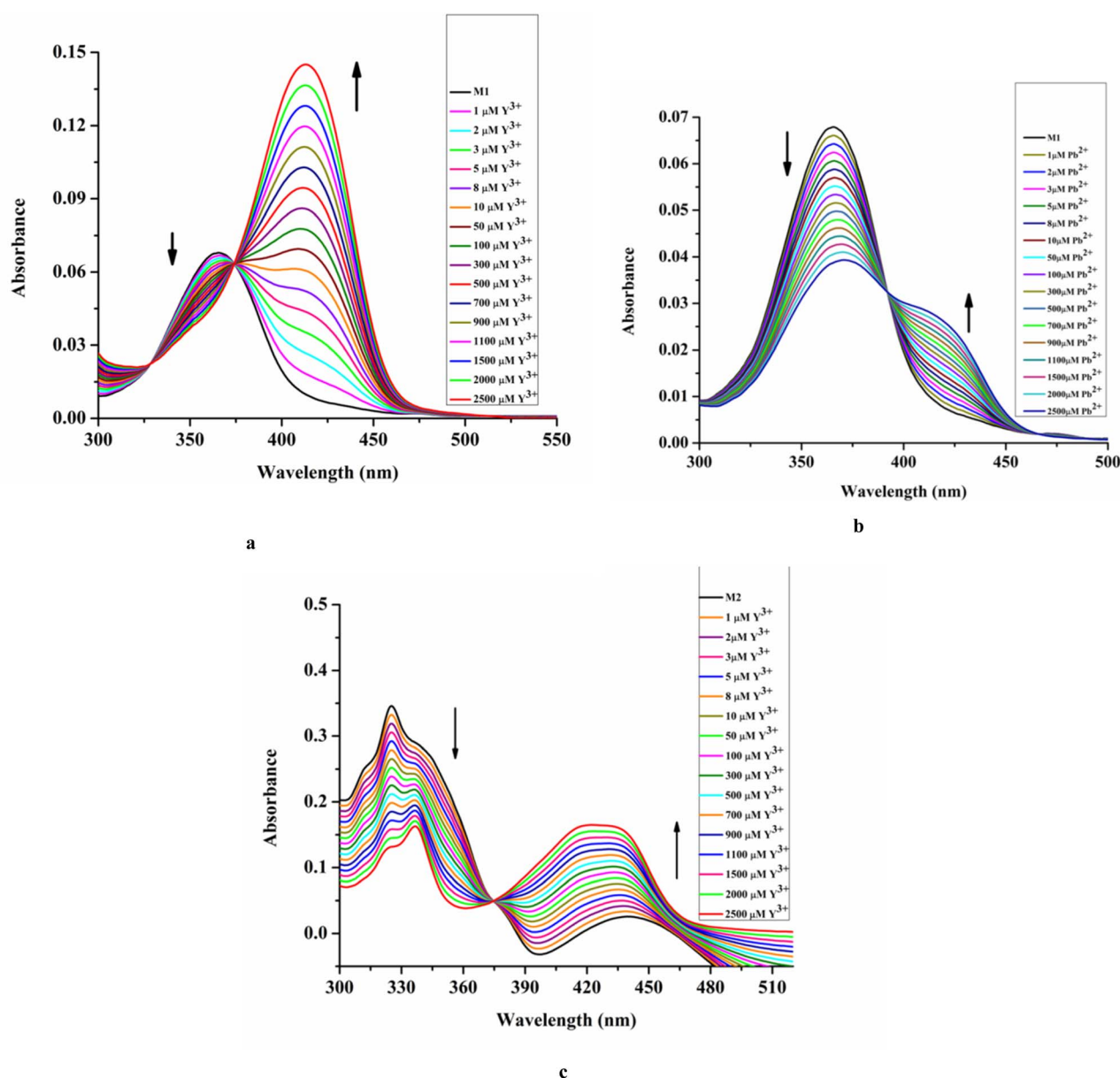

Fig. 2 UV-vis titration: **M1** (20 μM) *vs.* [M^{n+}] where M^n = Y^{3+} [0–2500 μM] (a) and Pb^{2+} [0–2500 μM] (b); **M2** (20 μM) *vs.* [Y^{3+}] [0–2500 μM] (c) HEPES buffered EtOH/H$_2$O (4/1, v/v, pH 7.4).

resulting in enhancement of OD value of lower wavelength peak and LMCT process for the intensified OD of higher wavelength peak.

Upon the addition of Y^{3+} to **M2**, the absorbance at a lower wavelength is reduced and shifted to 336 nm due to the change in environment. The presence of the electron rich $-ONO_2$ group might lower the intra-ligand charge transfer process. While the absorbance at a higher wavelength increases with a blue shift to 419 nm *via* an isosbestic point at 375 nm due to the LMCT process (Fig. 2c).

The structural beauty of **L1** having two types of functionalities, *viz.* imine moiety (with $-NEt_2$ and act as donor) and amide moiety (acts as acceptor) allow intra-ligand charge transfer (ILCT) process.[61] Such ILCT becomes more favourable at a particular geometry. Probably, upon complexation with metal ions, the **L1** gains rigidity and appropriate geometry for the ILCT process, resulting in a change in OD values. On the other hand, for **L2** devoid of donor groups like $-NEt_2$, the ILCT is poor. Upon complexation with a suitable metal ion, the LMCT process operates, leading to a change in OD values. The absence

or weak LMCT process in the case of **M1** might be due to the existence of a very strong ILCT process.

It has been observed that Y^{3+} and Pb^{2+} assisted "turn on fluorescence" of **M1** and Y^{3+} triggered fluorescence enhancement of **M2** is pH sensitive and demand monitoring at different pH (pH 2.0–12.0) [Fig. S9a–c, ESI].† The optimum performance has been observed near physiological pH, 7.4, which directed us to investigate the entire spectroscopic studies at pH 7.4 (EtOH/H_2O, 4/1, v/v, 10 mM HEPES buffer). It is noteworthy to mention that increasing the water percentage of aqueous ethanol reduces emission intensity.

Moreover, it has been observed that except Pb^{2+} and Y^{3+} other relevant common cations *viz.* Cu^{2+}, Cr^{3+}, Mn^{2+}, Fe^{2+}, Fe^{3+}, Co^{2+}, Ni^{2+}, Al^3, Zn^{2+}, Ag^+, Cd^{2+}, Hg^{2+}, La^{3+}, Ce^{4+}, Gd^{3+}, Tb^{3+}, and Dy^{3+} do not affect the emission intensity of **M1** ($\lambda_{ex} = 410$ nm) (Fig. 3a).

On the other hand, steady-state emission spectra of **M2** ($\lambda_{ex} = 342$ nm) are affected by Y^{3+} while other mentioned cations remain silent (Fig. 3b).
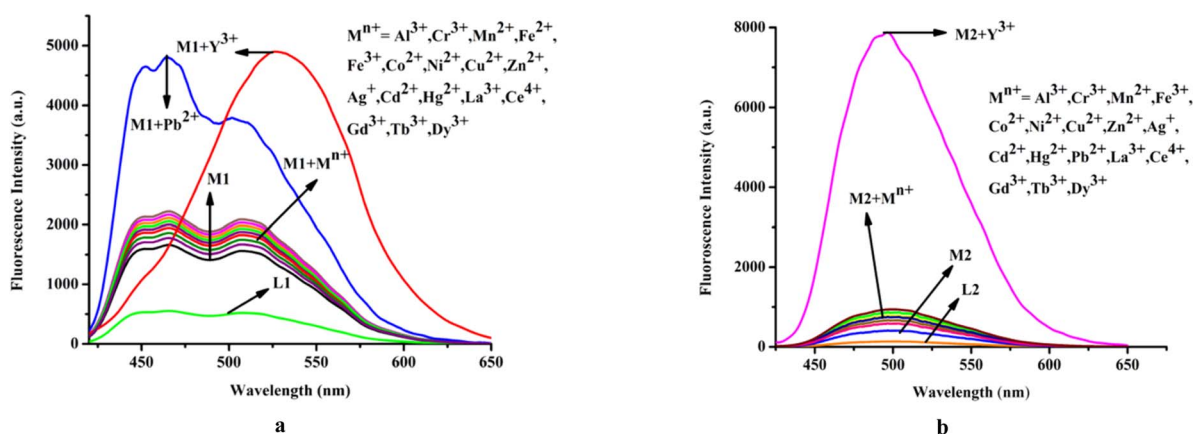

Fig. 3   Effect of common cations on emission spectra of (a) **M1** (20 μM) and (b) **M2**; media and pH mentioned earlier.
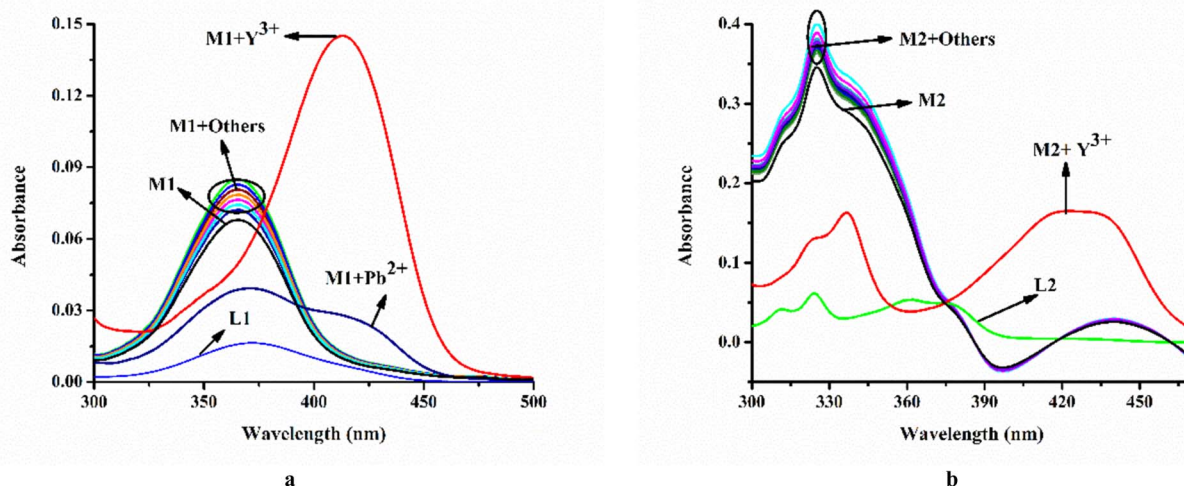

Fig. 4   Effect of common cations on absorption spectra of (a) **M1** (20 μM) and (b) **M2** (20 μM); media and pH mentioned *supra*.

The corresponding absorption spectroscopic studies are demonstrated in Fig. 4a and b.

In the presence of Y^{3+}, the emission intensity of **M1** changes in a ratiometric manner. Upon gradual increase of Y^{3+} concentration, emission intensity at 449 nm decreases while it increases significantly at 527 nm with an iso-emissive point at 468 nm (Fig. 5a). Fluorescence titration of **M1** with Pb^{2+} results in the enhancement of emission intensity at all wavelengths *viz.* at 449 nm, 463 nm, and 503 nm with increasing Pb^{2+} concentration (Fig. 5b). Similarly, the emission intensity of **M2** at 497 nm gradually enhances with increasing Y^{3+} concentration (Fig. 5c).

The selectivity of **M1** towards Y^{3+} and Pb^{2+} has been tested by measuring the emission intensities of **M1** in two separate mixtures containing Y^{3+} and Pb^{2+}, respectively, along with various other metal ions (Fig. S10a and b, ESI†). Likewise, the selectivity of **M2** for Y^{3+} has been verified by monitoring the emission intensity of **M2** in a mixture of Y^{3+} and various other common metal ions (Fig. S10c, ESI†). The presence of the mentioned common cations does not interfere with the emission intensities of **M1**-Y^{3+}, **M1**-Pb^{2+}, and **M2**-Y^{3+} systems, pointing out the selectivity of the recognition processes. The emission intensity *vs.* analyte concentration plot is sigmoidal (Fig. S11a–c, ESI†), the linear regions of which allow determining the limit of detection (LOD), the values of which for **M1** towards Y^{3+} and Pb^{2+} are 5.5×10^{-7} M and 26×10^{-9} M, respectively (Fig. S12a and b, ESI),† while for **M2** towards Y^{3+} is 8.0×10^{-7} M (Fig. S12c, ESI†). The corresponding association constants for **M1**-Y^{3+}, **M1**-Pb^{2+}, and **M2**-Y^{3+} systems are 3.9×10^4 M^{-1}, 2.9×10^4 M^{-1}, and 1.3×10^5 M^{-1}, respectively (Fig. S13a–c, ESI).† Job's plots indicate 1 : 1 stoichiometry for all the adducts *viz.* **Y1**, **Y2**, and **P1**, respectively (Fig. S14a–c, ESI).†

Interestingly, excitation spectroscopic studies (Fig. S17a–c†) provided an understanding of the molecular level interaction between the probes and sensed cations. In the case of **M1**, and in the presence of Y^{3+} (assigned as **Y1**), the excitation at the emission wavelength (527 nm) results in an excitation spectrum, which is split and the complex pattern does not allow us
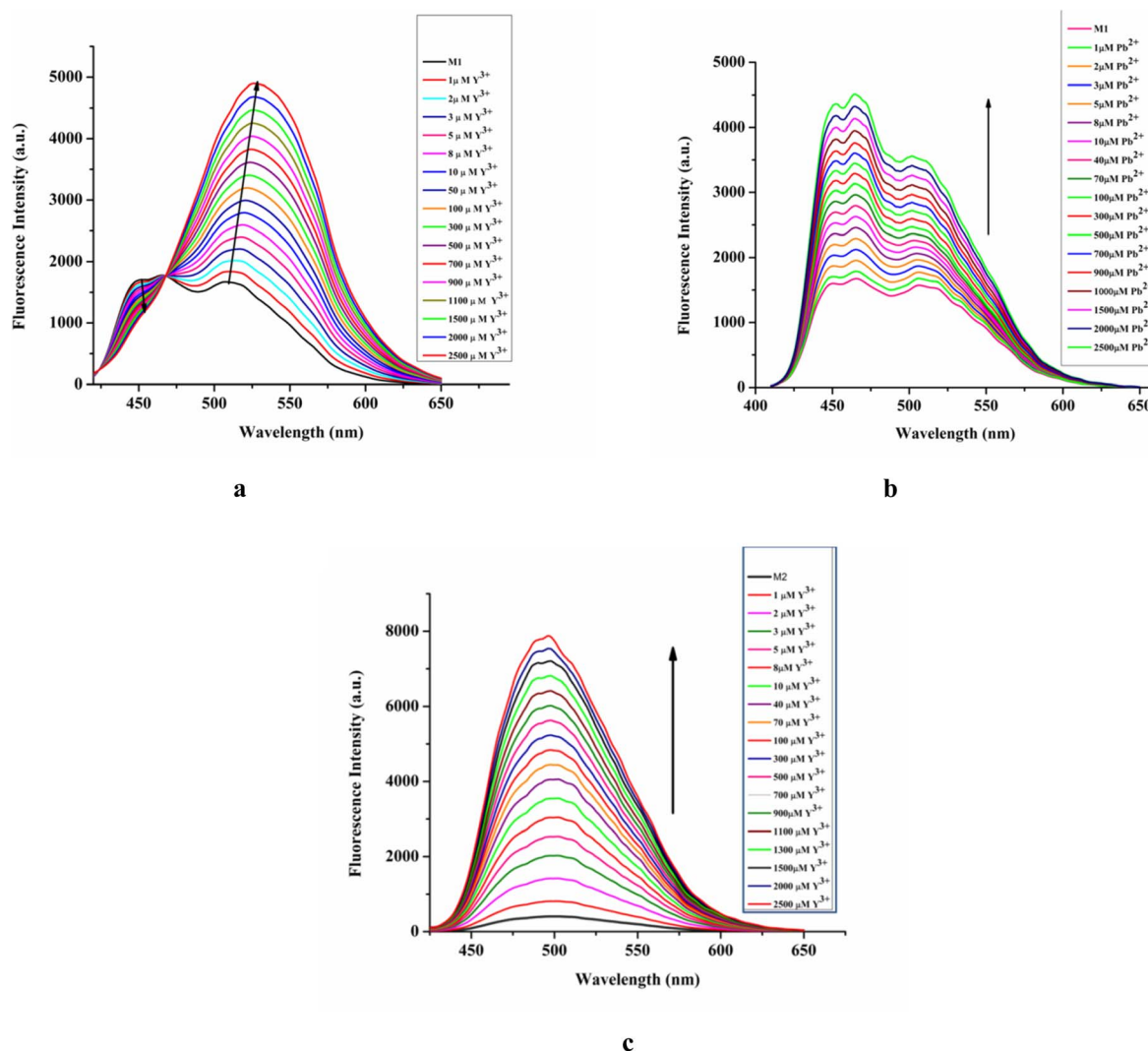

Fig. 5 Fluorescence titration of **M1** (20 μM) *vs.* [Y^{3+}] (a), [Pb^{2+}] (b), λ_{ex} = 410 nm; and **M2** (20 μM) *vs.* [Y^{3+}], λ_{ex} = 342 nm (c) media and pH mentioned *supra*.

to conclude about its aggregation. However, the excitation spectrum corresponding to the emission spectrum for the interaction of **M1** with Pb^{2+} (assigned as **P1**) undergoes a red-shift by 40 nm compared to its absorption spectrum, indicating *J* aggregation. In the case of **M2**, and in the presence of Y^{3+} (assigned as **Y2**), the excitation at the emission wavelength (497 nm) results in an excitation spectrum almost identical to its absorption spectrum, indicating no aggregation.

Sensing mechanism

The weak emissions of **L1** and **L2** is attributed to the photo-induced electron transfer (PET) process that arises from amide–N to –CH=N– moiety. Mo(VI) triggered inhibition of both PET and –CH=N– isomerization enhanced the rigidity leading to chelation enhanced fluorescence process (CHEF). The addition of Y^{3+} and/Pb^{2+} displaced Mo(VI) from corresponding Mo(VI) complexes leading to strong fluorescence. The fact is supported by the ESI-MS (*m/z*) spectra and single crystal X-ray structures of **M1** and **M2**. Further, Y^{3+} and Pb^{2+} triggered fluorescence enhancement of **M1** and **M2** have been rationalized by the metal displacement process where Mo(VI) is being replaced by Y^{3+} and Pb^{2+} ions[60] from their respective complexes, *viz.* **M1** and **M2** with the formation of **M1**-Y^{3+} (**Y1**), **M1**-Pb^{2+} (**P1**), and **M2**-Y^{3+} (**Y2**) adducts (Scheme 2). Replacement of Mo(VI) by Pb^{2+} from **M1** leads to **P1**, and supported by the corresponding ESI-MS spectrum, having (*m/z*), [M + H]$^+$, 595.1094. Job's plot in all three cases also corroborates these facts of 1 : 1 product formation (Fig. S14a–c, ESI).†

In spite of the similar orientation and geometry of the ligand prior and post-displacement of Mo(VI), the emission profile of all the systems are different. The explanation lies in the structure of **L1**, where ILCT is inherent. In the emission profile of **M1**, among two peaks, one is associated with the CT (at a lower wavelength) and the other is for the CHEF process. The process of charge transfer is favoured by the tetrahedral geometry of **P1** as compared to octahedral **M1**, and therefore, with the changeover of **P1** from **M1**, both the peaks associated with CT and CHEF are enhanced. Coming to **Y1**, the charge transfer is disfavoured and suppressed as compared to the process of CHEF, and hence a ratiometric

behaviour is observed. The lowering of the extent of charge transfer from donor to acceptor might be due to the presence of the electron rich –ONO$_2$ group in the complex **Y1**, and therefore the real donor becomes a pseudo donor. Hence the mutuality between the fluorophore donor and acceptor is no longer predominant here. This is the proposed explanation of experimental observation in the context of metal displacement in **M1** by Y^{3+} and Pb^{2+}. For **L2**, there is no ILCT as described *supra*; intensified emission is due to the CHEF process only that operates in a more active way than compared to its parent complex, **M2**.

Interestingly, probe **M1** is capable of dual sensing Y^{3+} and Pb^{2+}, while probe **M2** recognizes only Y^{3+}.

Upon moving from phenyl to naphthalene moiety (from **M1** to **M2**), the probe shows selectivity for Y^{3+} only. This fact may be rationalized in terms of the higher PET efficiency of naphthalene over the phenyl ring. This is also reflected in replacement kinetics, where we observed rapid replacement (almost instantaneous) of Mo(VI) by Pb^{2+} and Y^{3+} from **M1**, whereas it takes almost sixteen (16) s in the case of **M2** by Y^{3+}. The corresponding rate constants of the displacement reactions are 1.2×10^8 M^{-1} s^{-1}, 4.3×10^8 M^{-1} s^{-1}, and 6.3×10^5 M^{-1} s^{-1}, respectively. The slow displacement kinetics for the **M2**-Y^{3+} system probably indirectly implies higher selectivity of **M2** for Y^{3+}. In other words, the slow reactivity of **M2** over **M1** made it more inert than **M1** and hence allowed only Y^{3+}, but not Pb^{2+}, to interact. The metal displacement kinetics was monitored by the stopped-flow spectrophotometric method. Changes in absorbance at 426 nm for the **M1**-Pb^{2+} system, at 413 nm for the **M1**-Y^{3+} system and at 440 nm for the **M2**-Y^{3+} system are measured as a function of time. A pseudo first order kinetic behaviour is observed in all cases (Fig. S15a–c†). The sensing interaction is further rationalized by ^{1}HNMR titration, TCSPC, and DFT studies.

Comparison with other pioneering Y^{3+} and Pb^{2+} probes[62–71]

Trace level determination of Y^{3+} and Pb^{2+} using Mo(VI) complexes (**M1** and **M2**) by fluorescence method is compared with available pioneering probes and presented in Tables S1 and S2,[62–71] (ESI).† A closer look reveals that some probes may have better LOD but the method either involves fluorescence
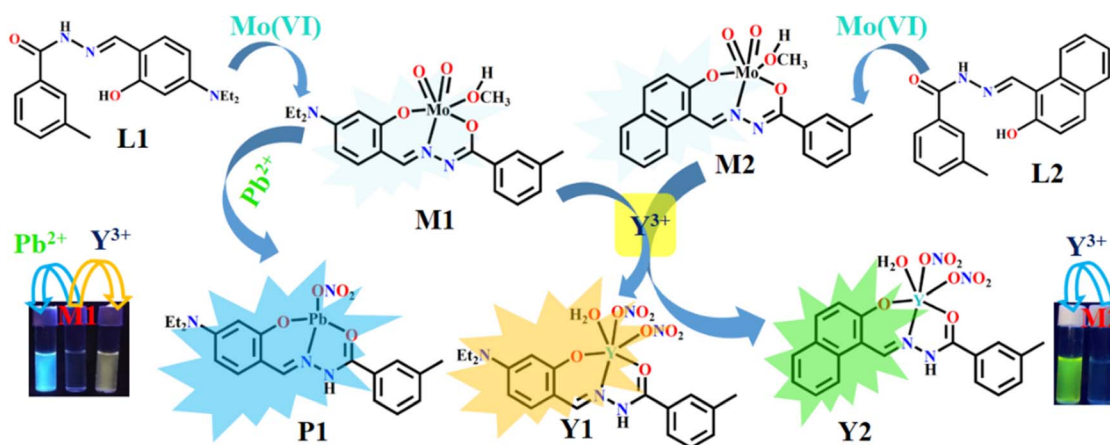
Scheme 2 Plausible sensing mechanism.

quenching, which is not at all desirable in sensing studies or toxic solvents like THF and CH$_3$CN. The present work has used a comparatively green solvent, EtOH.

^{1}HNMR titration

The interaction of metal ions with the organic probe and resulting metal complexes have been followed through ^{1}HNMR titration. Highly de-shielded amide proton (a) at 11.697 ppm and phenol –OH proton (b) at 11.405 ppm of **L1** fully disappeared upon complexation with Mo(VI), leading to the formation of **M1** (also established by single crystal X-ray structure) (Fig. S16a, ESI†). Notably, in the presence of both Y^{3+} and Pb^{2+}, the peak patterns of **M1** changed abruptly. New peaks appeared at 11.804 ppm and 11.878 ppm in the case of **Y1** (**M1-Y^{3+}**) and **P1** (**M1-Pb^{2+}**), respectively, similar to amide protons of **L1** (a1), supporting the proposed mechanism.

A similar observation was found for **M2** (Fig. S16b, ESI†) upon interaction with Y^{3+}.

Highly de-shielded amide proton (a′) at 12.733 ppm and phenol –OH proton (b′) at 12.115 ppm of **L2** disappeared upon complexation with Mo(VI), whereas the a′ proton reappeared at 12.714 ppm during *trans*-metallation of Mo(VI) by Y^{3+}.

Time correlated single photon counting studies (TCSPC studies)

The fluorescence life time decay experiment also corroborates the cation–probe interaction. Weakly fluorescent **M1** shows a characteristic decay profile in the presence of Y^{3+}, Pb^{2+}, while similar observation has been found for **M2** upon interaction with Y^{3+} at their respective emission wavelengths (Fig. 6). The average life time (τ) of adduct **Y1**, **P1**, and **Y2** are 1.73 ns, 3.35 ns, and 2.33 ns, respectively. The time-resolved fluorescence life time data are presented in Table 1.

Theoretical studies

To explore the underlying energy parameters of different frontier molecular orbitals involved in the process of probe-analyte interaction, density functional theoretical (DFT) studies have

Fig. 6 Fluorescence life time decay profiles of **Y1**, **P1**, and **Y2**.

Table 1 Fluorescence life time data of **Y1**, **P1**, and **Y2**

Species	B_1	B_2	τ_1 (ns)	τ_1 (ns)
Y1	82.55	17.45	0.026	1.83
P1	10.26	89.74	0.089	3.33
Y2	76.27	23.73	0.756	3.44

been performed with the **L1**, **L2**, **M1**, **M2**, **Y1**, **Y2**, and **P1** complexes/adducts using the basis set TD-SCF/DFT/B3LYP/SDD. The energy gap between the highest occupied molecular orbital (HOMO) and lowest unoccupied molecular orbitals (LUMO) for **L1**, **L2**, and **M1**, **M2**, **Y1**, **P1**, and **Y2** are shown in Fig. 7a and b, respectively. The HOMO–LUMO energy gaps in **L1** and **L2** are 0.04616 eV and 0.09488 eV, respectively, where the HOMO–LUMO energy gaps in **M1** and **M2** decrease to 0.03079 eV and 0.02278 eV. The corresponding values in **M1-Y^{3+}** and **M1-Pb^{2+}** are 0.02738 eV and 0.01783 eV, respectively, indicating the stability of **Y1** and **P1**. The corresponding value for **M2-Y^{3+}** (**Y2**) adduct is 0.01944 eV. Here, a slightly decreased energy gap of **M1** with respect to **L1** has been shown. However, the addition of Y^{3+} and Pb^{2+} to **M1** lowers the energy gap and is associated with a red shift, matching the experimental findings with theoretical values. In the case of **M2**, the energy gap decreased with respect to **L2**, which indicates the red shift of the absorption peak and clearly supports the experimental findings. The addition of Y^{3+} to **M2** also lowers the energy gap. Here, some anomalous behaviour of the absorption peak of **M1** with respect to **L1** has been observed where a blue shift occurs with a decrease in the energy gap. This type of mismatch of theoretical observation does not result in a less stable complex.[72–75] Fig. 7a and b also represent the electronic distribution in all the orbitals, which are in agreement with spin allowed electronic transition.

In the case of HOMO of **L1** and **L2**, the electron density is localized on benzene moiety and additionally along within the –NEt$_2$ group in **L1**. **M1**'s as well as **M2**'s HOMO shows a distribution of electron density towards the aromatic moiety mainly, whereas their LUMO electron density is totally confined on metal bound centres. **Y1** represents the transition of electron density from salicylaldehyde moiety (HOMO) to all over the complexes, especially up to the metal centre (LUMO). The HOMO of **P1** restricted the electron density to the metal bound centre where the electron density was distributed to the imine centre along with meta toluic acid moiety of **P1**'s LUMO.

Looking at the HOMO of **M1**, where the electron density is distributed in a dispersed way, the displacement of Mo(VI) by Pb^{2+} yields **P1**, which displays almost a homogeneous distribution of charge over the entire molecule. This outcome must be correlated with a strong operation of the CT process, as described earlier in the spectroscopic investigation. Interestingly, the ratiometric behaviour as obtained from the spectroscopy can also be interpreted with these MOs. In **Y1**, the distribution of charge, even in a dispersed way, no longer exists, and it might be due to the completely arrested CT process. Therefore, activation of the CHEF process along with this CT inhibition results in ratiometric behaviour.
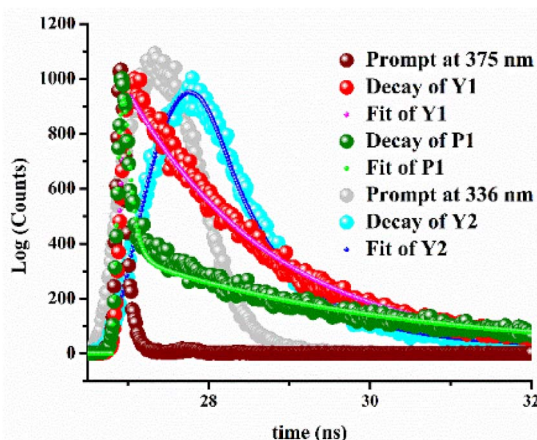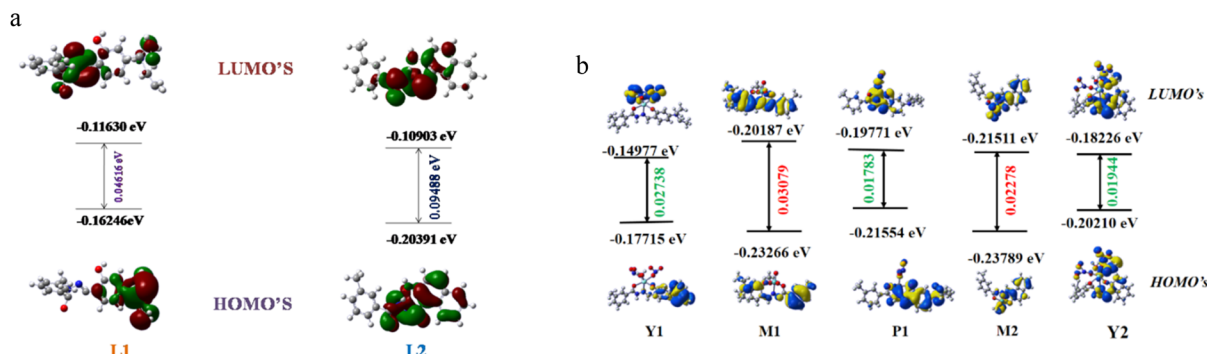
Fig. 7 (a) Frontier molecular orbitals along with HOMO–LUMO energy gaps of L1 and L2. (b) Frontier molecular orbitals along with HOMO–LUMO energy gaps of M1, M2, Y1 (M1-Y^{3+}), P1 (M1-Pb^{2+}) and Y2 (M2-Y^{3+}).
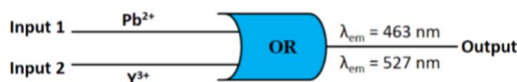

Fig. 8 General representation of the molecular logic circuit.

Table 2 Truth table of the logic gate operation

Input 1 (Pb^{2+})	Input 2 (Y^{3+})	Output (λ_{em} = 463 nm/527 nm)
0	0	0
0	1	1
1	0	1
1	1	1

Now **Y2**, where the distribution is only due to CHEF activation, shows a much greater electron density than **M2**. This indicates the intensified absorption/emission during the displacement of Mo(VI) by Y^{3+} from **M2**. Moreover, **Y2**'s HOMO cramped the electron density in naphthalene moiety, which gets transferred to the metal bound co-ordination zone of **Y2**'s LUMO. Such flow of electron density is associated with the charge transfer related electronic transition. All the above facts partially support the experimental findings.

Logic gate behaviour

The emission behaviour of **M1** at 463 nm and 527 nm in the presence of Pb^{2+} and Y^{3+} may be presented through "OR" logic gates (Fig. 8). By considering Pb^{2+} and Y^{3+} as input function and assuming turn on fluorescence as output (λ_{em} = 463 nm/527 nm) we can employ **M1** for the construction of a binary logic gate. In the case of input, "absence and presence" are denoted as "0" and "1", respectively, whereas for output, the allocations are "0" and "1" for weak and strong emissions, respectively. Truth table is shown in Table 2.

Conclusion

Two Mo(VI) complexes of amide–imine conjugate have been employed for selective recognition of Y^{3+} and Pb^{2+}. Y^{3+} and Pb^{2+} easily displace Mo(VI) from weakly fluorescent metal complex, **M1** whereas Mo(VI) is quickly displaced by Y^{3+} in **M2**. In the presence of Y^{3+} and Pb^{2+}, **M1** emits yellow and blue light, respectively, while **M2** selectively interacts with Y^{3+} to emit green fluorescence. The proposed sensing mechanism is based on the metal displacement protocol that has been substantiated by several spectroscopic and analytical techniques. Moreover, DFT studies established the stability of the resultant adducts, **Y1**, **P1**, and **Y2**, over respective Mo(VI) complexes.

Conflicts of interest

There are no conflicts to mention.

Acknowledgements

References

1 N. G. Connelly, T. Damhus, R. M. Hartshorn and A. T. Hutton, *Nomenclature of Inorganic Chemistry, IUPAC Recommendations*, RSC Publishing, 2005, p. 51.

2 J. Emsley, *Nature's Building Blocks: An A–Z Guide to the Elements*, Oxford University Press, 2001, pp. 495–498.

3 C. A. Hampel, *The Encyclopaedia of the Chemical Elements*, Reinhold Book Corporation, New York, 1968, pp. 810–821.

4 N. N. Greenwood and A. Earnshaw, *Chemistry of the Elements*, Butterworth-Heinemann, Oxford, 2nd edn, 1997.

5 C. R. Hammond, *The Elements*, Fermi National Accelerator Laboratory, 1985, pp. 4–33.

6 N. S. MacDonald, R. E. Nusbaum and G. V. Alexander, *J. Biol. Chem.*, 1952, **195**(2), 837–841.

7 G. P. Adams, C. C. Shaller, E. Dadachova, H. H. Simmons, E. M. Horak, A. Tesfaye, A. J. P. Klein-Szanto, J. D. Marks, M. W. Brechbiel and L. M. Weiner, *Cancer Res.*, 2004, **64**(17), 6200–6206.

8 A. Forssén, *Ann. Acad. Sci. Fenn., Ser. A*, 1974, (163), 1–4.

9 G. P. Adams, *Cancer Res.*, 2004, **64**, 6200–6206.

10 S. Raj and D. R. Shankaran, *Sens. Actuators, B*, 2016, **226**, 318–325.

11 Y. Shang, Y. Zhang, P. Li, J. Lai, X. Y. Kong, W. Liu, K. Xiao, G. Xie, Y. Tian and L. Wen, *Chem. Commun.*, 2015, **51**, 5979–5981.

12 J. Liu and Y. Lu, *J. Am. Chem. Soc.*, 2003, **125**, 6642–6643.

13 J. Y. Kwon, Y. J. Jang, Y. J. Lee, K. M. Kim, M. S. Seo, W. Nam and J. Yoon, *J. Am. Chem. Soc.*, 2005, **127**, 10107–10111.

14 Y. Q. Wen, C. Peng, D. Li, L. Zhuo, S. He, L. Wang, Q. Huang, Q. H. Xu and C. Fan, *Chem. Commun.*, 2011, **47**, 6278–6280.

15 M. Vazquezgonzalez and C. Carrillocarrion, *J. Biomed. Opt.*, 2014, **19**, 101503.

16 B. Sharma, S. Singh and N. J. Siddiqi, *BioMed Res. Int.*, 2014, **2014**, 640754.

17 G. Aragay, J. Pons and A. Merkoçi, *Chem. Rev.*, 2011, **111**, 3433–3458.

18 H. Wang, Y. Kim, H. Liu, Z. Zhu, S. Bamrungsap and W. Tan, *J. Am. Chem. Soc.*, 2009, **131**, 8221–8226.

19 B. Gu, L. Huang, N. Mi, P. Yin, Y. Zhang, X. Tu, X. Luo, S. Luo and S. Yao, *Analyst*, 2015, **140**, 2778–2784.

20 J. A. Cotruvo, *J.–Am. Water Works Assoc.*, 2017, **109**, 44–51.

21 G. A. Molander and F. Dehmel, *J. Am. Chem. Soc.*, 2004, **126**, 10313–10318.

22 J. W. B. Cooke, R. Bright, M. J. Coleman and K. P. Jenkins, *Org. Process Res. Dev.*, 2001, **5**, 383–386.

23 M. M. Gillett-Kunnath, J. G. MacLellan, C. M. Forsyth, P. C. Andrews, G. B. Deacon and K. Ruhlandt-Senge, *Chem. Commun.*, 2008, **37**, 4490–4492.

24 M. Lalonde, W. Bury, O. Karagiaridi, Z. Brown, J. T. Hupp and O. K. Farha, *J. Mater. Chem. A*, 2013, **1**, 5453–5468.

25 Y. A. Wanniarachchi, M. A. Khan and L. G. M. Slaughter, *Organometallics*, 2004, **23**, 5881–5884.

26 L. S. Felices, E. C. Escudero-Adán, J. Benet-Buchholz and A. W. Kleij, *Inorg. Chem.*, 2009, **48**, 846–853.

27 S. Akine, S. Sairenji, T. Taniguchi and T. Nabeshima, *J. Am. Chem. Soc.*, 2013, **135**, 12948–12951.

28 Y. Lou, Y. Zhao, J. Chen and J. J. Zhu, *J. Mater. Chem. C*, 2014, **2**, 595–613.

29 P. Wu, T. Zhao, S. Wang and X. Hou, *Nanoscale*, 2014, **6**, 43–64.

30 J. Rocha, L. D. Carlos, F. A. A. Paz and D. Ananias, *Chem. Soc. Rev.*, 2011, **40**, 926–940.

31 R. Xing, X. Wang, C. Zhang, J. Wang, Y. Zhang, Y. Song and Z. Guo, *J. Mater. Chem.*, 2011, **21**, 11142–11149.

32 A. C. Gyorkos, J. K. Stilleand and L. S. Hegedus, *J. Am. Chem. Soc.*, 1990, **112**, 8465–8472.

33 R. Cini, S. Defazio, G. Tamasi, M. Casolaro, L. Messori, A. Casini, M. Morpurgo and M. Hursthouse, *Inorg. Chem.*, 2007, **46**, 79–92.

34 Y. Zhu, E. Kockrick, T. Ikoma, N. Hanagata and S. Kaskel, *Chem. Mater.*, 2009, **21**, 2547–2553.

35 P. Horcajada, C. Serre, G. Maurin, N. A. Ramsahye, F. Balas, M. Vallet-Regí, M. Sebban, F. Taulelle and G. Férey, *J. Am. Chem. Soc.*, 2008, **130**, 6774–6780.

36 W. Plass and J. G. Verkade, *J. Am. Chem. Soc.*, 1992, **114**, 2275–2276.

37 E. C. Escudero-Adán, J. Benet-Buchholz and A. W. Kleij, *Inorg. Chem.*, 2007, **46**, 7265–7267.

38 I. Majumder, P. Chakraborty, S. Dasgupta, C. Massera, D. Escudero and D. Das, *Inorg. Chem.*, 2017, **56**, 12893–12901.

39 M. R. Maurya, S. Dhaka and F. Avecilla, *Polyhedron*, 2014, **67**, 145–159.

40 G. Arthur, *Biochemistry and Materials Science*, Wiley-Inter Science, 2000.

41 J. M. Humphrey and A. R. Chamberlin, *Chem. Rev.*, 1997, **97**, 2243–2266.

42 X. Liu, L. Lin and X. Feng, *Chem. Commun.*, 2009, 6145–6158.

43 S. Ta, M. Ghosh, N. Salam, S. Ghosh, P. Brandão, V. Félix, S. K. Hira, P. P. Manna and D. Das, *ACS Appl. Bio Mater.*, 2019, **2**, 3964–3973.

44 S. Ta, M. Ghosh, K. Ghosh, P. Brandão, V. Félix, S. K. Hira, P. P. Manna and D. Das, *ACS Appl. Bio Mater.*, 2019, **2**, 2802–2811.

45 M. Banerjee, S. Ta, M. Ghosh and A. G. D. Das, *ACS Omega*, 2019, **4**, 10877–10890.

46 J. M. C. Pavbn, M. E. U. Pozo, A. G. de Torres and C. B. Ojeda, *Analyst*, 1988, **113**(8), 1291–1294.

47 L. Li, M. de G. J. Peláez, E. A. Sarduy, X. Wang, T. E. Barnhart, W. Cai, V. Radchenko, P. Schaffer, J. W. Engle and C. Orvig, *Dalton Trans.*, 2020, **49**, 5547–5562.

48 N. Koslowski, R. C. Hoffmann, V. Trouillet, M. Bruns, S. Foro and J. J. Schneider, *RSC Adv.*, 2019, **9**, 31386–31397.

49 D. F. Wood and M. R. Adams, *Analyst*, 1970, **95**, 556–561.

50 Y. Shen, W. Li, J. Wu, S. Li, H. Luo, S. Dai and W. Wu, *Dalton Trans.*, 2014, **43**(26), 10023–10032.

51 K. Okamoto and S. Fukuzumi, *J. Am. Chem. Soc.*, 2004, **126**(43), 13922–13923.

52 R. Zhou, B. Li, N. Wu, G. Gao, J. You and J. Lan, *Chem. Commun.*, 2011, **47**, 6668–6670.

53 J. Yang, C. Zhou, C. Liu, Y. Li, H. Liu, Y. Li and D. Zhu, *Analyst*, 2012, **137**, 1446–1450.

54 M. Liu, X. Lou, J. Du, M. Guan, J. Wang, X. Ding and J. Zhao, *Analyst*, 2012, **137**, 70–72.

55 Z. E. Jacobi, L. Li and J. Liu, *Analyst*, 2012, **137**, 704–709.

56 M. C. Burla, R. Caliandro, M. Camalli, B. Carrozzini, G. L. Cascarano, L. De Caro, C. Giacovazzo, G. Polidori and R. Spagna, *J. Appl. Crystallogr.*, 2005, **38**, 381–388.

57 G. M. Sheldrick, *Acta Crystallogr., Sect. E: Struct. Rep. Online*, 2008, **64**, 112–122.

58 G. M. Sheldrick, *Acta Crystallogr., Sect. A: Found. Crystallogr.*, 2015, **71**, 3–8.

59 O. V. Dolomanov, L. J. Bourhis, R. J. Gildea, J. A. K. Howard and H. Puschmann, *J. Appl. Crystallogr.*, 2009, **42**, 339–341.

60 J. Cheng, X. Zhou and H. Xiang, *Analyst*, 2015, **140**, 7082.

61 A. Vogler and H. Kunkely, *Coord. Chem. Rev.*, 2007, **251**, 577–583.

62 J. M. C. Pavón, M. E. U. Pozo, A. G. de Torres and C. B. Ojeda, *Analyst*, 1988, **113**(8), 1291–1294.

63 G. Ghodake, S. Shinde, R. G. Saratale, A. Kadam, G. D. Saratale and D. Y. Kim, *Colloids Surf., B*, 2019, **183**, 110436.

64 D. Zhang, Z. Zang, X. Zhou, Y. Zhou, X. Tang, R. Wei and W. Liu, *Inorg. Chem. Commun.*, 2009, **12**, 1154–1156.

65 M. Shen, C. M. Li, D. Na, Z. Q. Hao, X. Y. Li, L. B. Guo, Y. F. Lu and X. Y. Zeng, *J. Anal. At. Spectrom.*, 2018, **33**, 658–662.

66 D. F. Wood and M. R. Adams, *Analyst*, 1970, **95**(1131), 556–561.

67 X. Meng, D. Cao, Z. Hu, X. Han, Z. Li and W. Ma, *RSC Adv.*, 2018, **8**(59), 33947–33951.

68 F. Zapata, A. Caballero, A. Espinosa, A. Tárraga and P. Molina, *J. Org. Chem. Res.*, 2009, **74**(13), 4787–4796.

69 A. K. Shaily, I. Parveen and N. Ahmed, *Luminescence*, 2018, **33**, 713–721.

70 A. Thakur, D. Mandal and S. Ghosh, *Anal. Chem.*, 2013, **85**(3), 1665–1674.

71 J. Yang, C. Zhou, C. Liu, Y. Li, H. Liu, Y. Li and D. Zhu, *Analyst*, 2012, **137**(6), 1446–1450.

72 Z. Li, W. Chen, L. Dong, Y. Song, R. Li, Q. Li, D. Qu, H. Zhang, Q. Yang and Y. Lia, *New J. Chem.*, 2020, **44**, 3261–3267.

73 K. C. Song, H. Kim, K. M. Lee, Y. Sup Lee, Y. Do and M. H. Lee, *Sens. Actuators, B*, 2013, **176**, 850–857.

74 S. Sinha, B. Chowdhury and P. Ghosh, *Inorg. Chem.*, 2016, **55**, 9212–9220.

75 J. Wu, W. Liu, J. Ge, H. Zhang and P. Wang, *Chem. Soc. Rev.*, 2011, **40**, 3483–3495.